

Variational formulation of marine ice-sheet and subglacial-lake grounding-line dynamics

Aaron G. Stubblefield¹,†, Marc Spiegelman^{1,2} and Timothy T. Creyts¹

(Received 7 April 2020; revised 8 April 2021; accepted 30 April 2021)

Grounding lines exist where land-based glacial ice flows on to a body of water. Accurately modelling grounding-line migration at the ice-ocean interface is essential for estimating future ice-sheet mass change. On the interior of ice sheets, the shores of subglacial lakes are also grounding lines. Grounding-line positions are sensitive to water volume changes such as sea-level rise or subglacial-lake drainage. Here, we introduce numerical methods for simulating grounding-line dynamics in the marine ice sheet and subglacial-lake settings. Variational inequalities arise from contact conditions that relate normal stress, water pressure and velocity at the base. Existence and uniqueness of solutions to these problems are established using a minimisation argument. A penalty method is used to replace the variational inequalities with variational equations that are solved using a finite-element method. We illustrate the grounding-line response to tidal cycles in the marine ice-sheet problem and filling-draining cycles in the subglacial-lake problem. We introduce two computational benchmarks where the known lake volume change is used to measure the accuracy of the numerical method.

Key words: ice sheets, variational methods, computational methods

1. Introduction

In Antarctica, grounded ice goes afloat on the ocean to create a series of ice shelves. The characterisation and health of these ice shelves has received intense study because they can restrain the flow of grounded ice through buttressing (Paolo, Fricker & Padman 2015; Fürst et al. 2016; Pegler 2018). The transition from ice being in contact with the bed to floating on water is called the grounding line. Grounding-line dynamics are closely tied to the stability and evolution of marine ice sheets (Schoof 2007a, 2012; Gudmundsson et al. 2012). For example, satellite data show that rapid grounding-line retreat is occurring at

† Email address for correspondence: aaron@ldeo.columbia.edu

¹Lamont-Doherty Earth Observatory, Columbia University, Palisades, NY, USA

²Department of Applied Physics and Applied Math, Columbia University, New York, NY, USA

Pine Island Glacier and Thwaites Glacier in the Amundsen Sea region of West Antarctica, probably owing to sub-shelf melting and unstable bed geometry (Rignot et al. 2014; Milillo et al. 2019). While models predict that this rapid migration will result in accelerated mass loss in the future, the timing and magnitude of such change is uncertain (Favier et al. 2014; Joughin, Smith & Medley 2014). Accurately modelling grounding-line response to climatic forcings is essential for forecasting land-ice contributions to sea-level rise.

Sea-level change causes grounding-line migration on both long and short time scales. Satellite altimetry shows that ocean tides cause diurnal cycles in ice-shelf surface elevation and flexure near the grounding line (Fricker & Padman 2006; Sykes, Murray & Luckman 2009; Brunt et al. 2010). Variability in the inland limit of elevation change over time suggests that grounding-line positions are also sensitive to tidal cycles (Brunt, Fricker & Padman 2011). Tidal flexure and grounding-line migration can cause variations in ice-flow speed by modulating stresses and friction at the base (Gudmundsson 2007; Sergienko, MacAyeal & Bindschadler 2009; Robel et al. 2017; Rosier & Gudmundsson 2020).

A similar setting where grounding lines occur is on the shores of subglacial lakes. Numerous subglacial lakes have been identified beneath the Antarctic ice sheet through a variety of geophysical methods (Wright & Siegert 2012). When the water volume of a subglacial-lake changes, the ice surface above the lake responds accordingly. Anomalies in surface-elevation changes have been to used to detect over one hundred actively filling or draining subglacial lakes (Smith et al. 2009). Observations of subglacial-lake filling and draining events provide information about the dynamics of the subglacial hydrological system (Fricker & Scambos 2009; Smith et al. 2017; Siegfried & Fricker 2018). Modelling the ice response to lake volume change requires consideration of grounding-line migration, but this has not been included in previous studies (Pattyn 2008; Gudlaugsson et al. 2016).

Models for marine ice sheets based on approximations to the Stokes equations have been developed, analysed and supported by laboratory experiments (Weertman 1974; Muszynski & Birchfield 1987; MacAyeal 1989; Schoof 2007a,b; Robison, Huppert & Worster 2010; Schoof 2012; Pegler & Worster 2013; Pegler et al. 2013; Seroussi et al. 2014). More recently, the full Stokes equations have been used to simulate the dynamics of marine ice sheets (Durand et al. 2009a,b; Favier et al. 2012; Gudmundsson et al. 2012; Gagliardini et al. 2016; Cheng, Lötstedt & von Sydow 2020). On tidal time scales, nonlinear viscoelastic models have been used (Rosier, Gudmundsson & Green 2014; Rosier & Gudmundsson 2020). In these models, conditions on the normal stress and velocity at the lower boundary determine whether ice remains in contact with the bed or goes afloat. However, previous methods consider the contact conditions after discretisation rather than include them in the variational problem.

While the marine ice sheet and subglacial-lake problems are similar, there are two important differences. The first difference is that subglacial lakes have finite volume, whereas the ocean volume is unbounded relative to the sub-shelf cavity volume. The second difference is that the normal-stress boundary condition at the ice-water interface can be well approximated a priori in the marine ice-sheet problem because sub-shelf water is connected to the sea surface. In contrast to previous studies, we do not assume that the subglacial-lake water pressure equals the cryostatic pressure (Pattyn 2008; Gudlaugsson et al. 2016). Instead, we show later that the mean water pressure is part of the solution to the problem and is constrained by water volume conservation.

In this paper, we derive and test numerical methods for grounding-line dynamics in the marine ice sheet and subglacial-lake settings. In contrast to previous studies, we incorporate the contact conditions directly into the variational formulations of the problems. After describing the domain and governing equations (§§ 2.1 and 2.2), we derive expressions for water pressure (§ 2.3) and discuss the boundary conditions (§ 2.4). Following a standard approach in contact mechanics, we show that the problems may be cast as variational inequalities posed over a set of admissible velocity fields (§ 3.1). We introduce minimisation formulations of the problems to establish well-posedness and justify the penalty method (§ 3.2). We then derive the penalty formulations (§ 3.3) that are solved numerically with a finite-element method (§ 3.4). To illustrate the numerical method, we provide examples of grounding-line response to tidal cycles in the marine ice-sheet problem ($\S 4.1$) and filling-draining cycles in the subglacial-lake problem ($\S 4.2$).

2. Model description

2.1. Domain

We consider a body of water beneath an ice sheet in the plane. We denote the spatial coordinate by x = (x, z). We assume the lower boundary of the ice is described by a function s(x, t) that is bounded below by the bed, $\beta(x)$. We define h(x, t) to be the surface elevation of the ice sheet. The ice-filled domain is defined by

$$\Omega = \{(x, z) : |x| < L/2, \ s(x, t) < z < h(x, t)\},$$
(2.1)

for a constant length L. As we are mainly concerned with modelling ice flow near the grounding lines, the length L is arbitrary but much smaller than the length of the ice sheet. We let Γ_w and Γ_b be the ice-water and ice-bed surfaces, respectively. These boundaries are defined by

$$\Gamma_{w} = \{(x, z) \in \partial \Omega : z = s(x, t) > \beta(x)\},\tag{2.2}$$

$$\Gamma_b = \{ (x, z) \in \partial \Omega : z = s(x, t) = \beta(x) \}, \tag{2.3}$$

$$\Gamma_s = \Gamma_w \cup \Gamma_b, \tag{2.4}$$

where Γ_s denotes the entirety of the lower boundary. Grounding lines exist where the ice-water and ice-bed boundaries meet. We let the minimum and maximum grounding-line positions be $x_{-}(t)$ and $x_{+}(t)$, respectively. We use x_{\pm} to collectively refer to both grounding lines. We assume that the subglacial-lake water is not connected to the surface, although this is not true for all glacial lakes. The model geometry for both settings is illustrated in figure 1.

2.2. Ice flow

Here, we outline the ice-flow component of the model. We let u be the ice velocity, pthe ice pressure, ρ_i the ice density and η the ice viscosity. We denote the horizontal and vertical components of a vector v by v_x and v_z , respectively. We assume that ice deforms as an incompressible viscous fluid subject to the Stokes equations

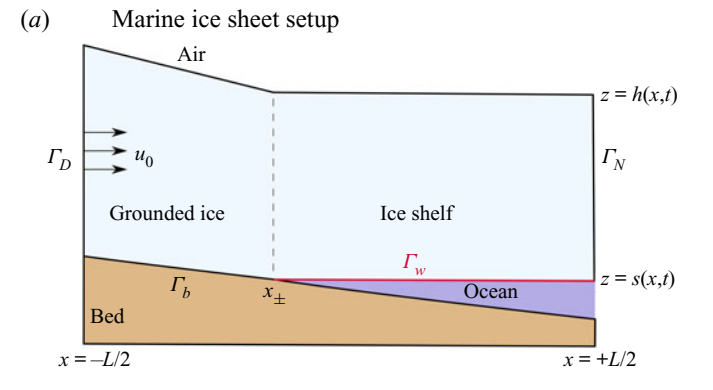
$$-\nabla \cdot \boldsymbol{\sigma}(\boldsymbol{u}, p) = \rho_i \boldsymbol{g}, \tag{2.5}$$

$$\nabla \cdot \boldsymbol{u} = 0, \tag{2.6}$$

where $\mathbf{g} = g[0, -1]^{\mathrm{T}}$ is gravitational acceleration with magnitude g. Momentum conservation and incompressibility are ensured through (2.5) and (2.6), respectively.



A.G. Stubblefield, M. Spiegelman and T.T. Creyts



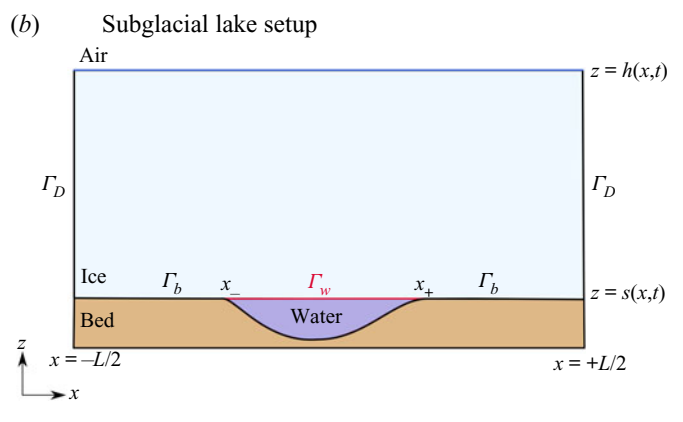


Figure 1. (a) Model geometry for the marine ice-sheet problem, highlighting the boundaries defined in §§ 2.1 and 2.4. The horizontal inflow speed is noted by $u_0 > 0$. (b) Model geometry for the subglacial-lake problem. We consider zero inflow and outflow ($u_0 = 0$) in this setting.

The stress is related to pressure and velocity through

$$\sigma(u, p) = -pI + 2\eta(u)D(u), \tag{2.7}$$

where

$$\mathbf{D}(\mathbf{u}) = \frac{1}{2} \left[\nabla \mathbf{u} + (\nabla \mathbf{u})^{\mathrm{T}} \right]$$
 (2.8)

is the strain rate and I is the identity matrix. Throughout, we use the Frobenius norm $|\mathbf{D}| = \sqrt{\mathbf{D} : \mathbf{D}}$ for tensors. Defining $n \ge 1$ to be the stress exponent and A > 0 the ice softness, we use Glen's law to relate the viscosity to the strain rate through the equation

$$\eta(\mathbf{u}) = \frac{1}{2}B(|\mathbf{D}(\mathbf{u})|^2 + \delta)^{(r-2)/2},$$
(2.9)

where r = 1 + 1/n and $B = 2^{(n-1)/2n}A^{-1/n}$ are flow law parameters (Glen 1955; Cuffey & Paterson 2010). The parameter $\delta \ll 1$ is used to prevent infinite viscosity at zero strain rate in numerical simulations (Jouvet & Rappaz 2011; Helanow & Ahlkrona 2018). While ice has a viscoelastic rheology on the tidal time scales explored in § 4.1, we consider the purely viscous rheology here to illustrate the numerical method and provide a point of comparison for studies that include elasticity.

The evolution of the upper and lower surfaces are governed by the kinematic equations

$$\frac{\partial h}{\partial t}(x,t) = \sqrt{1 + \left(\frac{\partial h}{\partial x}\right)^2} u_n(x,h,t),\tag{2.10}$$

$$\frac{\partial s}{\partial t}(x,t) = -\sqrt{1 + \left(\frac{\partial s}{\partial x}\right)^2} u_n(x,s,t), \tag{2.11}$$

where

$$u_n = \mathbf{u} \cdot \mathbf{n}|_{\partial \Omega} \tag{2.12}$$

is the normal component of the velocity on the boundary and n is the outward-pointing unit normal to the boundary (Durand et al. 2009a; Schoof 2011). We neglect mass change at the surface (e.g. accumulation or ablation) and bed (e.g. melting or freezing) in (2.10) and (2.11), respectively, in order to focus on the mechanical contact problems.

2.3. Water pressure and volume change

We assume that both the ocean and subglacial lake are hydrostatic. We let p_w be the water pressure at the ice-water interface, with p_w^o and p_w^l denoting the particular expressions for the ocean and subglacial lake, respectively. For marine ice sheets, the hydrostatic water pressure is $p_w^o = \rho_w g(\ell - s)$, where ℓ is sea level. However, using the elevation s computed from the velocity solution at the previous time step is numerically unstable (Durand et al. 2009a). We approximate s at the current time step by applying the backward Euler method to (2.11) under the assumption of small gradients, $(\partial s/\partial x)^2 \ll 1$, to yield

$$s_*(x,t) = s(x,t-\Delta t) - (\Delta t)u_n(x,s,t),$$
 (2.13)

where Δt is the time-step size. Using the approximation s_* , the sub-shelf water pressure becomes

$$p_w^o(x, s, t) = \rho_w g(\ell(t) - s_*(x, t)). \tag{2.14}$$

Subglacial lakes have finite volume that can change considerably over time. The subglacial-lake volume \mathcal{V} evolves according to

$$\dot{\mathcal{V}}(t) = -\int_{\Gamma_s} u_n \, \mathrm{d}s. \tag{2.15}$$

For a prescribed volume change rate, equation (2.15) acts as an integral constraint on the normal component of the velocity at the base. In contrast, the marine ice-sheet problem does not have a constraint such as (2.15) because the ocean volume is larger than the sub-shelf cavity volume. In the marine case, the water volume change is instead controlled by the ice-flow response to water pressure variations, analogous to models of subglacial cavitation (Schoof 2005; Gagliardini et al. 2007).

We assume that subglacial-lake water is not connected to the surface, so there is no datum where water pressure is known a priori. Assuming hydrostatic balance ($\nabla p_w =$ $\rho_{w}\mathbf{g}$), the expression for water pressure is only determined up to a constant. Therefore, we choose to express the subglacial-lake water pressure as $p_w^l = \rho_w g(\bar{s} - s) + \bar{p}_w$, where \bar{s} and \bar{p}_w are the means of s and p_w^l over (x_-, x_+) . Although we expect that the water pressure is near the cryostatic pressure as assumed in previous models, determining \bar{p}_w is part of the solution to the problem (Pattyn 2008; Gudlaugsson et al. 2016). In the following,

we show that approximating \bar{p}_w by the mean cryostatic pressure is accurate within a few kilopascals. However, the utility of leaving \bar{p}_w undetermined is that it acts as a Lagrange multiplier that enforces the volume-change constraint (§ 3.1).

We also require a numerically stable approximation of the subglacial-lake water pressure. We may replace Γ_s with Γ_w in (2.15) by applying Leibniz's rule to $\mathcal{V}=$ $\int_{x}^{x_{+}} s - b \, dx$ if $x_{-}(t)$ and $x_{+}(t)$ are continuously differentiable. Although this smoothness assumption may not hold in general, we use it as an approximation in the stabilising scheme. Taking the mean of (2.13), we approximate $\bar{s}(t)$ at the current time step by

$$\bar{s}_*(t) = \bar{s}(t - \Delta t) + (\Delta t)\dot{\mathcal{V}}/|\Gamma_w|, \tag{2.16}$$

where we have assumed $-\int_{\Gamma_w} u_n \, ds \approx \dot{\mathcal{V}}$ and denoted the measure of Γ_w by $|\Gamma_w|$. Using the approximations (2.13) and (2.16), we arrive at the expression for subglacial-lake water pressure

$$p_w^l(x, s, t) = \rho_w g(\bar{s}_*(t) - s_*(x, t)) + \bar{p}_w(t).$$
(2.17)

We omit time arguments for brevity.

2.4. Boundary conditions

Stress continuity at the ice-water boundary implies

$$\boldsymbol{\sigma}\boldsymbol{n} = -p_{w}\boldsymbol{n} \quad \text{on } \Gamma_{w}, \tag{2.18}$$

where p_w is given by either (2.14) or (2.17), depending on the setting. Equation (2.18) implies that the shear stress vanishes on the ice-water boundary. We assume a stress-free condition at the ice-air interface, which requires that

$$\sigma n = 0 \quad \text{on } z = h(x, t). \tag{2.19}$$

On the inflow and outflow boundaries, we consider two types of boundary conditions (figure 1). First, we prescribe a uniform horizontal velocity and zero vertical shear stress

where $u_0 \ge 0$ is the horizontal flow speed and $T = I - nn^{T}$ is an orthogonal projection on to the boundary. Here Γ_D coincides with the inflow boundary in the case $u_0 > 0$ (marine case), or both the inflow and outflow boundaries when $u_0 = 0$ (subglacial-lake case). In the marine case $(u_0 > 0)$, we assume a cryostatic normal-stress condition of the form

$$\boldsymbol{\sigma}\boldsymbol{n} = -\rho_i g(h - z)\boldsymbol{n} \quad \text{on } \Gamma_N, \tag{2.21}$$

where Γ_N coincides with the outflow boundary. These inflow and outflow conditions are noted in figure 1.

In the marine case, equating the normal stresses

$$\sigma_n = -\mathbf{n} \cdot \mathbf{\sigma} \, \mathbf{n}|_{\partial \Omega} \tag{2.22}$$

associated with (2.18) and (2.21), where Γ_N and Γ_w meet (see figure 1a) leads to the flotation condition

$$h = s + \frac{\rho_w}{\rho_i}(\ell - s) \quad (\equiv h_f) \tag{2.23}$$

in the limit $\Delta t \to 0$ ($s_* \to s$). We confirm in what follows that the ice-surface elevation near the outflow boundary remains close to h_f (§ 4.1).

On the ice—bed boundary, we assume a sliding law of the form

$$T\sigma n + \alpha(u)Tu = 0 \quad \text{on } \Gamma_b$$
 (2.24)

with friction α given by

$$\alpha(\mathbf{u}) = C(|\mathbf{T}\mathbf{u}|^2 + \delta)^{(r-2)/2},$$
 (2.25)

where C > 0 is the friction coefficient and |a| denotes the Euclidean norm of a vector a (Weertman 1957; Kamb 1970). In the friction law (2.25), we assume the same value of regularisation parameter δ as in the flow law (2.9).

There are three possibilities for the normal stress σ_n and normal component of the velocity u_n at the ice-bed boundary. The first possibility is that the normal stress exceeds the water pressure $(\sigma_n > p_w)$ and the ice is not lifted off of the bed $(u_n = 0)$. The second possibility is that the ice is lifted from the bed $(u_n < 0)$ and the normal stress equals the water pressure $(\sigma_n = p_w)$ (Durand *et al.* 2009*a*; Schoof 2011). The third possibility is that the normal stress reaches the water pressure $(\sigma_n = p_w)$, but the ice is not lifted from the bed $(u_n = 0)$. These three cases are represented by either

$$\begin{cases}
\sigma_n \geqslant p_w \\
u_n = 0
\end{cases} \quad \text{or} \quad \begin{cases}
\sigma_n = p_w \\
u_n \leqslant 0
\end{cases} \quad \text{on } \Gamma_b. \tag{2.26}$$

The two sets of conditions in (2.26) are equivalent to

$$\begin{cases}
\sigma_n \geqslant p_w \\
u_n \leqslant 0 \\
(\sigma_n - p_w)u_n = 0
\end{cases}$$
on Γ_b . (2.27)

The contact conditions (2.27) are analogous to those in the Signorini problem from elasticity (Kikuchi & Oden 1988). We refer to the condition $u_n \leq 0$ as bed impenetrability.

3. Weak formulations

3.1. Derivation of mixed formulations

We now derive weak formulations of the models. We let V and Q be appropriate function spaces for the velocity and pressure, respectively (Appendix A.1). We define the set of admissible velocity fields by

$$K = \{ v \in V : v_n |_{\Gamma_D} \le 0 \text{ and } v_x |_{\Gamma_D} = u_0 \},$$
 (3.1)

which is a closed, convex subset of V. We let $v \in K$ be an arbitrary test function, multiply (2.5) by v - u and integrate by parts to obtain

$$\int_{\Omega} 2\eta(\mathbf{u}) \mathbf{D}(\mathbf{u}) : \mathbf{D}(\mathbf{v} - \mathbf{u}) - \rho_i \mathbf{g} \cdot (\mathbf{v} - \mathbf{u}) - p \nabla \cdot (\mathbf{v} - \mathbf{u}) \, \mathrm{d}\mathbf{x} - \int_{\partial \Omega} \sigma \mathbf{n} \cdot (\mathbf{v} - \mathbf{u}) \, \mathrm{d}\mathbf{s} = 0,$$
(3.2)

where we used the identity D(u): $\nabla(v-u) = D(u)$: D(v-u).

We turn our attention to the boundary integral over Γ_b . Using $\sigma n = T \sigma n - \sigma_n n$, the sliding law (2.24) and the identity $Tu \cdot (v - u) = Tu \cdot T(v - u)$ (since T is an orthogonal projection), we obtain

$$-\int_{\Gamma_b} \boldsymbol{\sigma} \boldsymbol{n} \cdot (\boldsymbol{v} - \boldsymbol{u}) \, \mathrm{d}s = \int_{\Gamma_b} \alpha(\boldsymbol{u}) \boldsymbol{\tau} \boldsymbol{u} \cdot \boldsymbol{\tau} (\boldsymbol{v} - \boldsymbol{u}) \, \mathrm{d}s + \int_{\Gamma_b} \sigma_n(v_n - u_n) \, \mathrm{d}s. \tag{3.3}$$

The contact conditions (2.27) and $v_n|_{\Gamma_h} \leq 0$ imply that

$$\int_{\Gamma_h} \sigma_n(v_n - u_n) \, \mathrm{d}s \leqslant \int_{\Gamma_h} p_w(v_n - u_n) \, \mathrm{d}s. \tag{3.4}$$

Combining inequality (3.4) with (3.2)–(3.3) and the boundary conditions (2.18)–(2.21), we obtain the variational inequality

$$\int_{\Omega} \left[2\eta(\boldsymbol{u}) \boldsymbol{D}(\boldsymbol{u}) : \boldsymbol{D}(\boldsymbol{v} - \boldsymbol{u}) - \rho_{i} \boldsymbol{g} \cdot (\boldsymbol{v} - \boldsymbol{u}) - p \nabla \cdot (\boldsymbol{v} - \boldsymbol{u}) \right] d\boldsymbol{x} + \int_{\Gamma_{s}} p_{w}(v_{n} - u_{n}) ds
+ \int_{\Gamma_{h}} \alpha(\boldsymbol{u}) \boldsymbol{T} \boldsymbol{u} \cdot \boldsymbol{T}(\boldsymbol{v} - \boldsymbol{u}) ds + \int_{\Gamma_{N}} \rho_{i} g(h - z)(v_{n} - u_{n}) ds \geqslant 0.$$
(3.5)

To simplify notation, we write

$$\mathcal{F}(\boldsymbol{u}, \boldsymbol{v}) = \int_{\Omega} \left[2\eta(\boldsymbol{u}) \boldsymbol{D}(\boldsymbol{u}) : \boldsymbol{D}(\boldsymbol{v}) - \rho_{i} \boldsymbol{g} \cdot \boldsymbol{v} \right] d\boldsymbol{x} + \int_{\Gamma_{b}} \alpha(\boldsymbol{u}) \boldsymbol{T} \boldsymbol{u} \cdot \boldsymbol{T} \boldsymbol{v} ds$$

$$+ \int_{\Gamma_{N}} \rho_{i} g(h - z) v_{n} ds$$
(3.6)

$$b_{\Omega}(q, \mathbf{u}) = \int_{\Omega} q \nabla \cdot \mathbf{u} \, \mathrm{d}\mathbf{x},\tag{3.7}$$

for $u, v \in V$ and $q \in Q$, which constitute the usual weak forms in Stokes ice-flow models. We also define

$$\mathcal{P}_{w}^{o}(\boldsymbol{u},\boldsymbol{v}) = \rho_{w}g \int_{\Gamma_{s}} \left[\ell - s + (\Delta t)u_{n}\right] v_{n} \,\mathrm{d}s, \tag{3.8}$$

$$\mathcal{P}_{w}^{l}(\boldsymbol{u},\boldsymbol{v}) = \rho_{w}g \int_{\Gamma_{s}} [\overline{s} - s + (\Delta t)(u_{n} + \dot{\mathcal{V}}/|\Gamma_{w}|)]v_{n} \,\mathrm{d}s, \tag{3.9}$$

$$b_{\Gamma}(q_w, \mathbf{u}) = -\int_{\Gamma_s} q_w u_n \,\mathrm{d}s,\tag{3.10}$$

for $u, v \in V$ and $q_w \in \mathbb{R}$, which originate from the weak forms of the ocean water pressure (2.14), subglacial-lake water pressure (2.17) and lake volume-change constraint (2.15), respectively. In (3.8) and (3.9), s and \bar{s} are known from the previous time step (§ 2.3).

We supplement inequality (3.5) with the weak form of incompressibility (3.7) and sub-shelf water pressure (3.8) to arrive at the mixed variational problem for marine ice sheets. We seek $(u, p) \in K \times Q$ such that

$$\begin{cases}
\mathcal{F}(\boldsymbol{u}, \boldsymbol{v} - \boldsymbol{u}) + \mathcal{P}_{w}^{o}(\boldsymbol{u}, \boldsymbol{v} - \boldsymbol{u}) - b_{\Omega}(\boldsymbol{p}, \boldsymbol{v} - \boldsymbol{u}) \geqslant 0 \\
b_{\Omega}(\boldsymbol{q}, \boldsymbol{u}) = 0
\end{cases}$$
(3.11)

for all $(v, q) \in K \times Q$. Similarly, the variational problem for subglacial lakes is to find $(\boldsymbol{u}, p, \bar{p}_w) \in K \times Q \times \mathbb{R}$ such that

$$\begin{cases}
\mathcal{F}(\boldsymbol{u}, \boldsymbol{v} - \boldsymbol{u}) + \mathcal{P}_{w}^{l}(\boldsymbol{u}, \boldsymbol{v} - \boldsymbol{u}) - b_{\Omega}(\boldsymbol{p}, \boldsymbol{v} - \boldsymbol{u}) - b_{\Gamma}(\bar{p}_{w}, \boldsymbol{v} - \boldsymbol{u}) \geqslant 0 \\
b_{\Omega}(\boldsymbol{q}, \boldsymbol{u}) + b_{\Gamma}(\boldsymbol{q}_{w}, \boldsymbol{u}) = \boldsymbol{q}_{w}\dot{\mathcal{V}}
\end{cases}$$
(3.12)

for all $(v, q, q_w) \in K \times Q \times \mathbb{R}$. In deriving (3.12), we used the subglacial-lake volume-change constraint (2.15) and the expression for water pressure (2.17). The form of (3.12) shows that the mean water pressure \bar{p}_w acts as a Lagrange multiplier that enforces the volume-change constraint, analogous to p enforcing incompressibility; we elaborate on this in the context of the penalty formulation in § 3.3.

3.2. Minimisation formulation

We now introduce minimisation formulations of problems (3.11) and (3.12) that justify the penalty methods discussed in the following section. We denote the set of divergence-free admissible velocity fields that obey the volume-change constraint by

$$K_{\star} = \{ \boldsymbol{u} \in K : b_{\Omega}(q, \boldsymbol{u}) + b_{\Gamma}(q_{w}, \boldsymbol{u}) = q_{w}\dot{\mathcal{V}} \text{ for all } (q, q_{w}) \in Q \times \mathbb{R} \},$$
 (3.13)

which is a closed, convex subset of V (Appendix A.2). On this subset, the mixed variational problem (3.12) reduces to finding $u \in K_{\star}$ such that

$$\mathcal{F}(\boldsymbol{u}, \boldsymbol{v} - \boldsymbol{u}) + \mathcal{P}_{w}^{l}(\boldsymbol{u}, \boldsymbol{v} - \boldsymbol{u}) \geqslant 0$$
(3.14)

for all $v \in K_{\star}$. For the sake of clarity, we set the regularisation parameter to $\delta = 0$ in the flow law (2.9) and sliding law (2.25). The results below still hold for $\delta > 0$ (Jouvet & Rappaz 2011). The left side of (3.14) is the Gâteaux derivative of the functional

$$\mathcal{J}(\boldsymbol{v}) = \int_{\Omega} \frac{B}{r} |\boldsymbol{D}(\boldsymbol{v})|^r - \rho_i \boldsymbol{g} \cdot \boldsymbol{v} \, d\boldsymbol{x} + \int_{\Gamma_b} \frac{C}{r} |\boldsymbol{T} \boldsymbol{v}|^r \, d\boldsymbol{s} + \int_{\Gamma_N} \rho_i g(h - z) v_n \, d\boldsymbol{s}$$
$$+ \rho_w g \int_{\Gamma_s} \gamma_1 v_n^2 + (\gamma_2 - s) v_n \, d\boldsymbol{s}$$
(3.15)

in the direction $\mathbf{v} - \mathbf{u}$, where $\gamma_1 = \Delta t/2$ and $\gamma_2 = \dot{\mathcal{V}} \Delta t/|\Gamma_w| + \bar{s}$.

The problem of minimising \mathcal{J} (3.15) over K_{\star} is equivalent to solving variational inequality (3.14) (Kikuchi & Oden 1988, Theorem 3.7). The functional \mathcal{J} is convex, continuous and coercive (Appendix A.2). These properties ensure that a minimiser $u \in K_{\star}$ of \mathcal{J} exists (Ekeland & Temam 1999, Proposition 1.2). Uniqueness follows from the strict convexity of \mathcal{J} (Chen, Gunzburger & Perego 2013, Lemmas 9 and 12). Therefore, there exists a unique solution u to the reduced problem (3.14). Existence and uniqueness of the corresponding pressures p and \bar{p}_w in the mixed formulation (3.12) follow from an inf–sup condition on the constraint operators b_{Ω} and b_{Γ} (Appendix A.3). Existence and uniqueness of solutions to the marine ice-sheet problem follows the same argument applied to the functional \mathcal{J} , with $\gamma_2 = \ell$, over the set of divergence-free admissible velocity fields.

3.3. Penalty formulation

Working with the set K is inconvenient for arbitrary bed geometry. Instead, we introduce a penalty formulation that is posed over V. To enforce the impenetrability constraint, we introduce the penalty functional

$$\Pi(\mathbf{v}) = \int_{\Gamma_b} \frac{1}{2} \left(v_n^2 + v_n |v_n| \right) d\mathbf{s}. \tag{3.16}$$

The Gâteaux derivative of Π at u in a direction v is

$$\Pi'(\boldsymbol{u},\boldsymbol{v}) = \int_{\Gamma_b} (u_n + |u_n|) \, v_n \, \mathrm{d}s. \tag{3.17}$$

 Π and Π' are non-zero only when impenetrability is violated (i.e. when $u_n > 0$). Therefore, $(1/\varepsilon)\Pi$ (and $(1/\varepsilon)\Pi'$) penalises $u_n > 0$ when the penalty parameter ε is chosen to be small. We seek $u \in V$ that minimises the penalised functional

$$\mathcal{J}_{\varepsilon}(\mathbf{v}) = \mathcal{J}(\mathbf{v}) + \frac{1}{\varepsilon} \Pi(\mathbf{v}), \tag{3.18}$$

and satisfies the relevant equality constraints, depending on the problem. Minimisers of $\mathcal{J}_{\varepsilon}$ converge weakly to minimisers of \mathcal{J} as $\varepsilon \to 0$, justifying the numerical method (Kikuchi & Oden 1988, Theorem 3.15).

To enforce the equality constraints, we introduce the Lagrangian for the marine problem

$$\mathcal{L}^{o}(\mathbf{v}, q) = \mathcal{J}_{\varepsilon}(\mathbf{v}) - b_{\Omega}(q, \mathbf{v}), \tag{3.19}$$

and for lake problem

$$\mathcal{L}^{l}(\mathbf{v}, q, q_{w}) = \mathcal{J}_{\varepsilon}(\mathbf{v}) - b_{\Omega}(q, \mathbf{v}) - b_{\Gamma}(q_{w}, \mathbf{v}) + q_{w}\dot{\mathcal{V}}, \tag{3.20}$$

where the pressures $(q, q_w) \in Q \times \mathbb{R}$ have been reintroduced as Lagrange multipliers. The solutions (u, p) to the marine problem and (u, p, \bar{p}_w) to the lake problem are saddle points of (3.19) and (3.20), respectively. We obtain the penalty formulations of (3.11) and (3.12) by taking Gâteaux derivatives of these Lagrangians (Kikuchi & Oden 1988, Theorem 3.13).

For the marine ice-sheet model, the penalised problem is to find $(u, p) \in V \times Q$, satisfying the Dirichlet condition, such that

$$\begin{cases} \mathcal{F}(\boldsymbol{u}, \boldsymbol{v}) + \mathcal{P}_{w}^{o}(\boldsymbol{u}, \boldsymbol{v}) - b_{\Omega}(p, \boldsymbol{v}) + \frac{1}{\varepsilon} \Pi'(\boldsymbol{u}, \boldsymbol{v}) = 0 \\ b_{\Omega}(q, \boldsymbol{u}) = 0 \end{cases}$$
(3.21)

for all $(\mathbf{v}, q) \in V_D \times Q$, where $V_D = {\mathbf{v} \in V : v_x | \Gamma_D = 0}$. Similarly, the subglacial-lake problem reduces to finding $(u, p, \bar{p}_w) \in V \times Q \times \mathbb{R}$ such that

$$\begin{cases} \mathcal{F}(\boldsymbol{u}, \boldsymbol{v}) + \mathcal{P}_{w}^{l}(\boldsymbol{u}, \boldsymbol{v}) - b_{\Omega}(p, \boldsymbol{v}) - b_{\Gamma}(\bar{p}_{w}, \boldsymbol{v}) + \frac{1}{\varepsilon} \Pi'(\boldsymbol{u}, \boldsymbol{v}) = 0 \\ b_{\Omega}(q, \boldsymbol{u}) + b_{\Gamma}(q_{w}, \boldsymbol{u}) = q_{w} \dot{\mathcal{V}} \end{cases}$$
(3.22)

for all $(v, q, q_w) \in V_D \times Q \times \mathbb{R}$. Variational problems (3.21) and (3.22) readily extend to three spatial dimensions; the details depend on the additional boundary conditions on the side walls of the domain, that must be chosen.

3.4. Numerical implementation

At each time step, we solve variational problem (3.21) or (3.22) with the finite-element package FEniCS (Logg, Mardal & Wells 2012; Alnæs et al. 2015). We use the Taylor-Hood element for velocity and pressure (Jouvet & Rappaz 2011). In the subglacial-lake case, the Taylor-Hood element is augmented with a Lagrange multiplier for $\bar{p}_w, q_w \in \mathbb{R}$, constituting a single additional global degree of freedom. We update the free surfaces h and s using (2.10) and (2.11) and the velocity solution, moving the boundary nodes of the mesh to obtain the new domain. The geometric constraint $s \ge \beta$ is then enforced explicitly. The interior nodes of the mesh are smoothed using the ALE (arbitrary Lagrangian–Eulerian) class in DOLFIN (Logg & Wells 2010; Logg et al. 2012). For the simulations discussed in § 4, we set the element width to 250 m at the upper

surface and refine it to $\Delta x = 12.5$ m at the lower surface. We choose the regularisation parameter $\delta = 10^{-15}$, flow law coefficient $B = 8.6 \times 10^7$ Pa s^{1/3}, flow law exponent r = 4/3, friction coefficient $C = 10^5$ Pa s^{1/3} m^{-1/3} and penalty parameter $\varepsilon = 10^{-13}$. The time-step sizes Δt for the different problems are provided subsequently. These parameters provide well-resolved and converged solutions (Appendix B.1).

In general, the true grounding-line positions exist between the mesh nodes. The numerical grounding-line positions depend on how the discretised ice-water (2.2) and ice-bed (2.3) boundaries are defined. Here, the discretised ice-bed boundary is defined as all element edges satisfying $s - \beta \leqslant \tau$ for a specified numerical tolerance τ , 1 mm for all examples herein. The discretised ice-water boundary includes all edges on the lower boundary satisfying $s - \beta > \tau$ and the edges where the true grounding lines exist (i.e. where $s - \beta - \tau$ changes sign). This choice of discretisation corresponds to the 'last-grounded' scheme in Gagliardini et al. (2016). Sub-grid parameterisations of the transition between these boundaries have been developed (Seroussi et al. 2014; Cheng et al. 2020). We do not explore these schemes here because they introduce additional terms in the weak forms that depend on the grounding-line positions. For plotting and convergence testing, we estimate the true grounding-line positions by linear interpolation between the mesh nodes. Throughout, we plot the interpolated positions rather than the adjacent mesh nodes where the discretised ice-water and ice-bed boundaries meet.

Verification and validation of the numerical model are established by providing a known subglacial-lake volume change rate. The computed results can then be compared with the true volume change and, in some cases, an expected grounding-line migration rate. Using this approach, we discuss convergence of the numerical method with decreasing ε , Δt and Δx (Appendix B.1). We provide a second benchmark test for validation that is based on an expected rate of grounding-line migration for a slow-filling triangular lake (Appendix B.2). For the marine problem, satisfaction of the flotation condition (2.23) near the outflow boundary is also a useful validation measure (figures 2 and 3). The code is openly available as an archived Git repository (Stubblefield 2020, doi:10.5281/zenodo.4302610).

4. Numerical examples

4.1. Tidal cycles

Here, we illustrate the grounding-line response to tidal cycles in the marine ice-sheet problem. We consider sinusoidal tidal cycles of the form

$$\ell(t) = \frac{\rho_i}{\rho_w} h_0 + \sin(2\pi t/P),\tag{4.1}$$

where the initial ice-shelf surface elevation is $h_0 = 500$ m, the period P is a half day and the maximum deviation from mean sea level $(\rho_i/\rho_w)h_0$ is 1m (figure 2). We choose a linear bed geometry

$$\beta(x) = -\frac{5x}{L},\tag{4.2}$$

where the length L=20 km. The inflow speed is set to $u_0=1$ km yr⁻¹ on Γ_D . We assume that the cryostatic condition (2.21) holds on the outflow boundary Γ_N (figure 1). To construct appropriate initial free surfaces for the tidal problem, we keep the sea level fixed at $\ell(t) = (\rho_i/\rho_w)h_0$ and evolve the initial conditions $s(x,0) = \max(\beta(x),0)$ and $h(x, 0) = h_0$ to time t = 0.35 yr, using a time-step size of $\Delta t = 5 \times 10^{-4}$ yr. The resulting

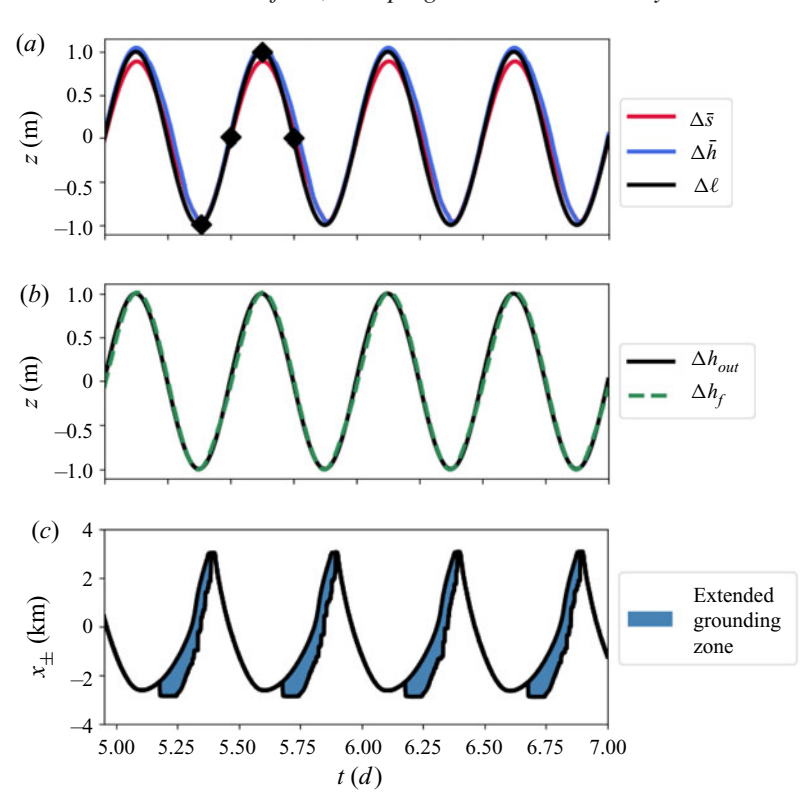


Figure 2. (a) Sea-level change $\Delta \ell = \ell(t) - \ell(0)$, mean ice–air elevation change $\Delta \bar{h} = \bar{h}(t) - \bar{h}(0)$ and mean ice-water elevation change $\Delta \bar{s} = \bar{s}(t) - \bar{s}(0)$ over the course of four tidal cycles, where \bar{h} and \bar{s} denote the mean of h and s over the ice-water boundary. The black diamonds mark the times and relative sea levels associated with the free-surface plots in figure 3. (b) Comparison of the outflow elevation $\Delta h_{out} = h(L/2, t) - h(L/2, 0)$ with the flotation elevation $\Delta h_f = h_f(t) - h_f(0)$, given by (2.23). (c) Minimum and maximum grounding-line positions over time. An extended grounding zone forms when sea level falls, characterised by the presence of a thin water layer between x_- and x_+ (discussed in § 4.1). The extended grounding zone is lost when sea level begins to rise, resulting in a single grounding line. We plot the results for $t \ge 5$ days after transients in the grounding-line time series have relaxed.

initial ice-sheet profile for the tidal simulation thickens inland from the shelf (figure 3a). For the tidal simulation, we reduce the time step to $\Delta t = 2 \times 10^{-6}$ yr to obtain a similar number of time steps per oscillation period as in the subglacial-lake problem where numerical accuracy has been verified. We explore numerical convergence and accuracy with respect to $(\Delta x, \Delta t)$ in Appendix B.1 and demonstrate that these solutions are well resolved in space and time.

The mean elevations of the ice-water interface and overlying ice-air interface closely follow the tidal cycle over time (figure 2a). At the outflow boundary, the ice elevation closely matches the flotation condition (2.23) that results from the stress boundary conditions (figure 2b). The grounding-line response is also periodic in time, migrating roughly 5 km over each cycle (figure 2c). The free-surface geometry over the course of one tidal cycle is shown in figure 3. We provide a movie of the complete simulation in the supporting information (supplementary movie 1). An intriguing feature of this solution is that, for oscillations on a tidal time scale, multiple contact points can form (figure 2c).

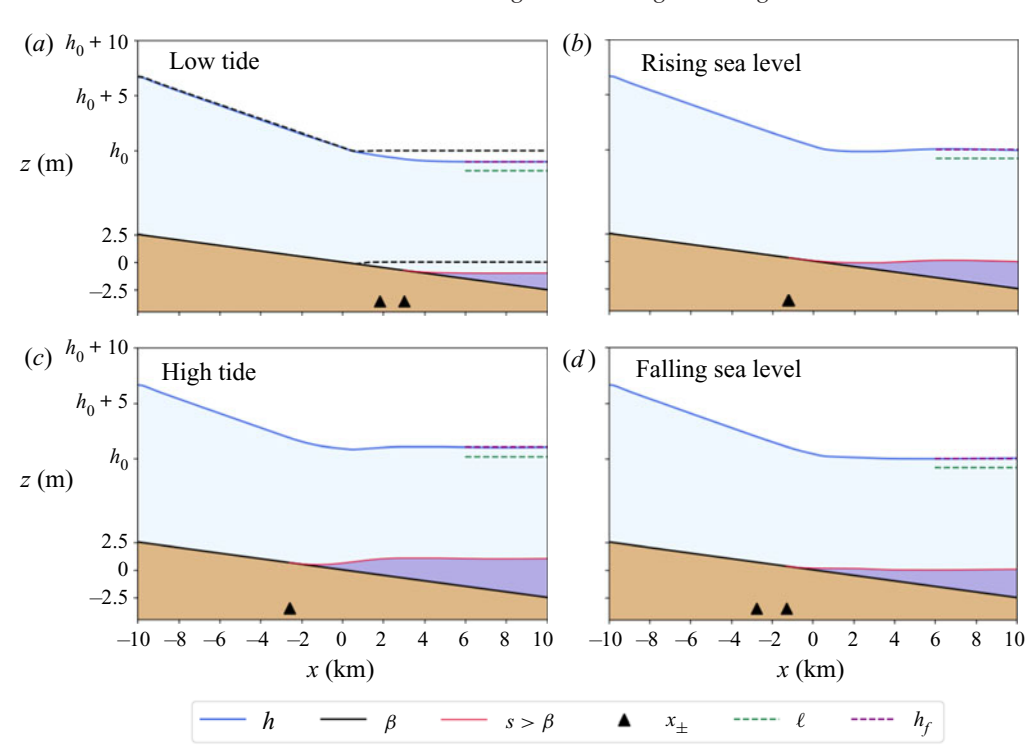


Figure 3. Plot of free-surface geometry over the course of one tidal cycle, with time increasing from (a-d). The times and relative sea levels are noted in figure 2(a). The initial geometry is depicted by dashed black lines in (a). Sea level ℓ is depicted by a dash-dotted green line and the ice-flotation elevation h_f (2.23) is depicted by a dashed purple line. For visualisation, 98 % of the initial sea-level and ice-surface elevation have been subtracted from ℓ and h, respectively. The reference upper surface elevation is $h_0 = 500$ m. The sea levels in (b,d) are the same. The colour scheme follows figure 1. The minimum and maximum grounding-line positions x_{\pm} are noted by black triangles.

The tidal cycle causes flexure in the ice sheet that leads to multiple contact points (figure 4). After high tide, ice begins to make contact with the bed as sea level falls. The strong downward flexure of the floating ice shelf causes an upward flexure inland of the main grounding line x_+ , which acts like a hinge (figure 4a). Ice is lifted from the bed in a zone adjacent to x_+ , forming a ~ 1 mm thick water layer of width ~ 1 km (figure 4b). We refer to this area of thin separation between ice and bed as the extended grounding zone. The upward flexure is balanced by a slight downward flexure farther inland that causes previously lifted patches of ice to progressively regain contact with the bed (figure 4a). This flexural response causes the thin water layer to migrate seaward behind the main grounding line x_+ while decaying in amplitude until low tide (figure 2c).

We show that the extended grounding zone forms for a wide range of mesh spacings in supplementary movie 2 ($\Delta x = 12.5$, 50 and 100 m), time-step sizes in supplementary movie 3 ($\Delta t = 1, 2$ and 4 min) and boundary geometry tolerances in supplementary movie 4 ($\tau = 10^{-2}$, 10^{-3} and 10^{-4} m). The width, maximum amplitude and migration speed of the water layer are insensitive to changes in these parameters. Therefore, the extended grounding zone is a robust feature of the solution. When the water layer collapses near low tide, differences between the solutions can occur on the sub-millimetre scale.

After low tide, the extended grounding zone is lost as ice is lifted off the bed by the rising sea (figures 2c, 3b). Only one grounding line exists as sea level rises because a

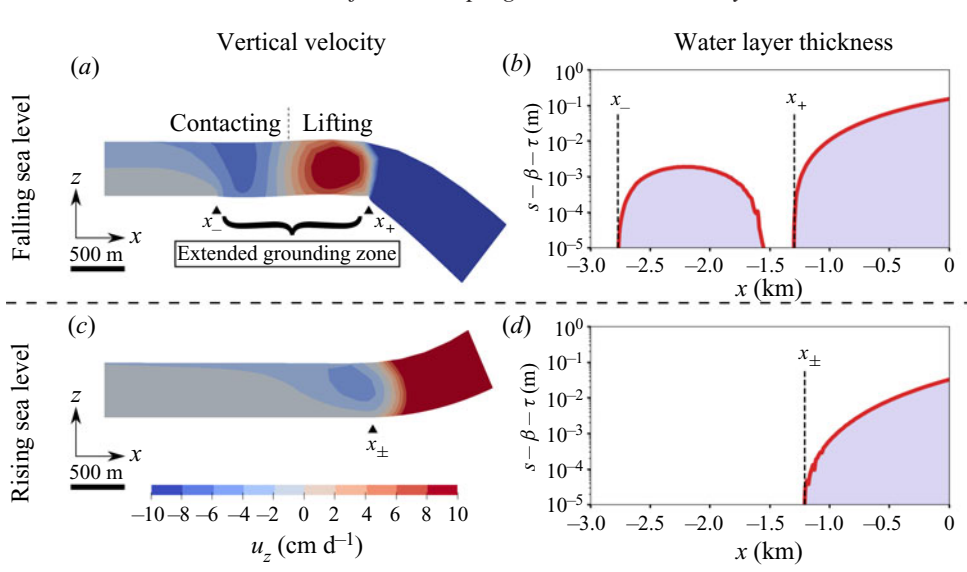


Figure 4. (a,c) Vertical velocity u_z near the grounding line plotted on the displaced mesh during the falling and rising stages of the tidal cycle. The times are noted in figure 2(a). The instantaneous displacement $u \times \Delta t$ has been exaggerated by a factor of $\sim 3 \times 10^5$ for visualisation. The width and structure of the extended grounding zone are noted in (a). Minimum and maximum grounding-line positions are noted by black triangles. (b,d)Water-layer thickness $s - \beta - \tau$ during the falling and rising stages of the tidal cycle, where τ is the boundary geometry tolerance parameter defined in § 3.4. (b) shows the \sim 1 mm thick water layer that forms between x_{-} and x₊. Supplementary movies 2–4 available at https://doi.org/10.1017/jfm.2021.394 show the evolution of the water-layer thickness over the full simulation for a range of numerical parameters.

downward flexure occurs inland of x_+ , balancing the strong upward flexure of the ice shelf (figure 4c,d). The grounding line migrates inland until high tide, when the cycle is completed. The extended grounding zone does not form at longer (e.g.weekly) oscillation periods because the flexural response is absent (supplementary movie 5).

4.2. Subglacial lake filling-draining cycles

Here, we illustrate grounding-line responses to subglacial-lake filling-draining cycles. Motivated by observations and modelling studies of sub-decadal cycles, we use a volume change rate \mathcal{V} obtained from a smoothed sawtooth volume-change time series with a period of one year (Fowler 2009; Kingslake 2015; Siegfried & Fricker 2018; Stubblefield et al. 2019). The volume change \mathcal{V} is shown in figure 5(a). We assume that the subglacial lake exists in a topographic low point on the bed beneath an ice slab of length L=10 km. Therefore, we let the bed topography be a Gaussian

$$\beta(x) = -10 \exp\left(-16\frac{x^2}{L^2}\right).$$
 (4.3)

We choose an initial lower surface given by $s(x, 0) = \max(\beta(x), -5 \text{ m})$, and a uniform initial upper-surface elevation of $h(x, 0) \equiv 1$ km (figure 6a). We set the horizontal inflow and outflow speeds to $u_0 = 0$ on $\Gamma_D = \{|x| = L/2\}$ so that $\Gamma_N = \emptyset$ (figure 1). We choose a time-step size of $\Delta t = 5 \times 10^{-4}$ yr.

The ice-air and ice-water surface-response time series mirror the sawtooth volume change (figure 5a,b). However, the upper-surface response is smaller in magnitude than

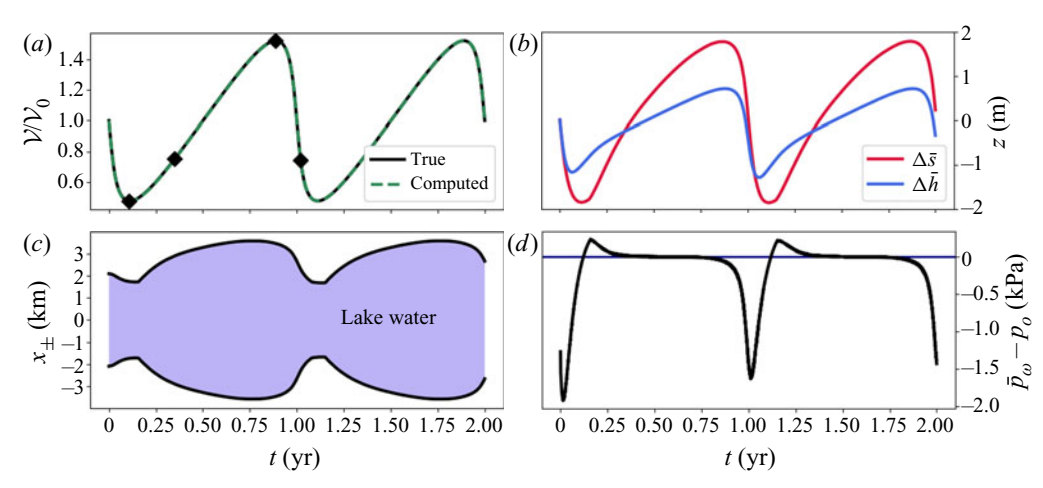


Figure 5. (a) Computed lake volume change V/V_0 compared with the exact volume change V_{true}/V_0 , where \mathcal{V}_0 is the initial lake volume. The black diamonds mark the times and relative water volumes associated with the free-surface plots in figure 6. (b) Change in mean values of h and s over the ice-water boundary (cf. figure 2a). The response of the upper surface is smaller in magnitude than that of the lower surface. (c) Motion of the grounding lines x_- and x_+ over time. (d) Plot of the deviation of the mean water pressure \bar{p}_w from the mean cryostatic pressure $p_o = \rho_i g(\bar{h} - \bar{s})$ over time. The line $\bar{p}_w = p_o$ is shown for reference.

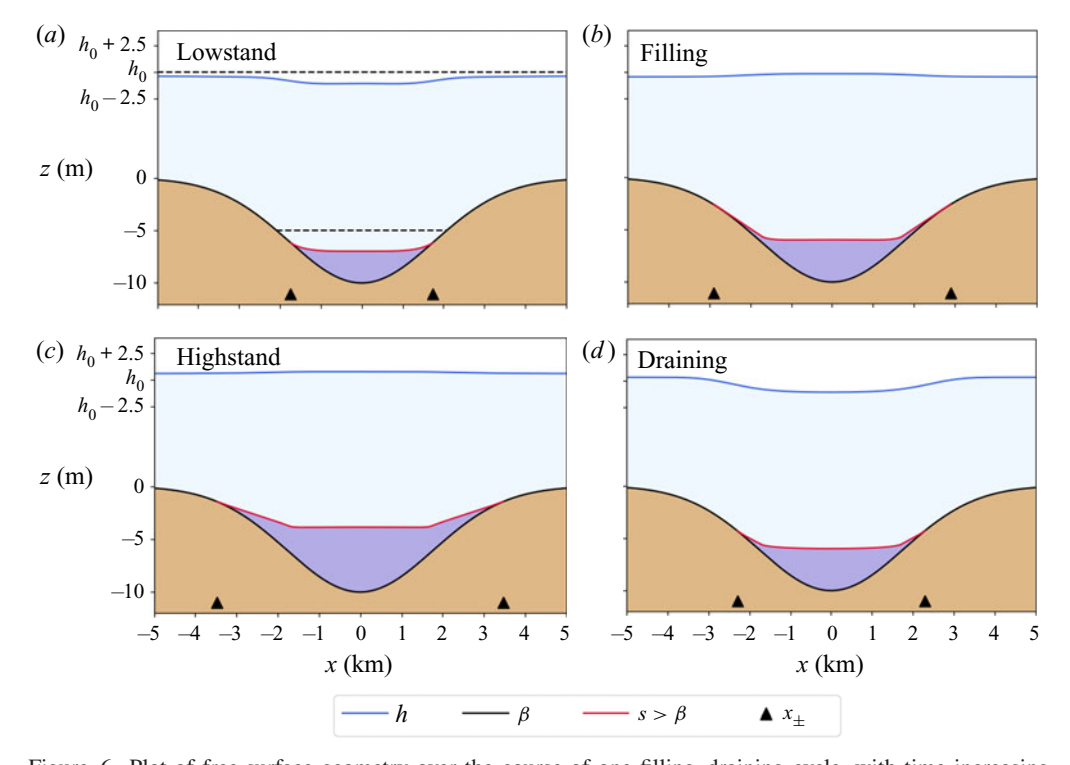


Figure 6. Plot of free-surface geometry over the course of one filling-draining cycle, with time increasing from (a-d). The reference upper-surface elevation is $h_0 = 1$ km and the initial geometry is depicted by dashed black lines in (a). For visualisation, 99% of the initial ice-surface elevation has been subtracted from h. The times and relative water volumes are noted in figure 5(a). The water volumes in (b,d) are the same. The colour scheme follows figure 1. The grounding-line positions x_+ are noted by black triangles.

the lower-surface response because it is distributed over a wider area. The grounding lines move inward and outward during the draining and filling stages, respectively (figure 5c). Both grounding lines migrate a total distance of \sim 1.9 km over the course of the cycle. We also plot the deviation of \bar{p}_w from the mean cryostatic pressure $p_o = \rho_i g(\bar{h} - \bar{s})$ over time (figure 5d). The difference $\bar{p}_w - p_o$ is slightly positive during the filling stage as the subglacial water forces the ice upwards. During the draining stage, the cryostatic pressure exceeds the water pressure by up to \sim 2 kPa because the water is not fully supporting the weight of the ice.

We show the spatial pattern of elevation change and grounding-line migration over one filling-draining cycle in figure 6. The elevations of the grounding lines remain close to the mean elevation of the ice-water interface \bar{s} during lake lowstand and the draining stages (figure 6a,d). During the filling stage, the grounding lines move outward as the ice separates from the bed (figure 6b,c). The grounding-line elevations quickly surpass the mean elevation \bar{s} , leaving only a thin gap between the ice and the bed initially (figure 6b). Over the time scale considered here, the lower surface deforms to the shape of the bed so that it records the lowest elevation experienced during the draining stage. At slower volume change rates, this crack-like geometry near the grounding lines does not develop because the lower surface can relax viscously (Appendix B.2). As before, we provide a movie of the complete simulation (supplementary movie 6).

5. Discussion

In the tidal problem, we described the formation of a thin water layer that extends the grounding zone farther inland during sea level fall. The extended grounding zone results from flexural bending of the ice, which occurs on short time scales in thin viscous sheets (Ribe 2001). Sayag & Worster (2013) showed that tidal bending can generate oscillations in the hydraulic gradient near the grounding line, potentially providing a similar mechanism for the formation of isolated subglacial water bodies. Similarly, Warburton, Hewitt & Neufeld (2020) explored how coupling between elastic bending, dynamic water pressure and subglacial drainage can influence tidal grounding-line migration. Determining the dynamic coupling between grounding-line migration and subglacial drainage at the ice—ocean interface remains a pertinent area for future work.

An advantage of our subglacial-lake model compared with previous work is that ice flow is directly linked to the volume change rate. Subglacial-lake volume change is controlled by the inflow and outflow of water through drainage pathways such as channels, canals, cavities and water sheets (Nye 1976; Walder & Fowler 1994; Fowler 1999; Creyts & Schoof 2009; Hewitt, Schoof & Werder 2012; Schoof, Hewitt & Werder 2012; Stubblefield et al. 2019). This formulation provides a natural coupling of ice flow to subglacial hydrology models because the volume change rate can be expressed as the net inflow or outflow of water from drainage elements that are connected to the lake. As the mean water pressure \bar{p}_w closely approximates the mean cryostatic pressure p_o , the effective pressure is $p_0 - p_w = \rho_w g(s - \bar{s}) + O(1 \text{ kPa})$ (figure 5d). This relation can serve as an effective pressure boundary condition in subglacial hydrology models, perhaps with a correction to account for underpressure during draining stages. We leave further exploration of the ice-flow response to lake volume change for future work since this probably depends on the choice of lateral boundary conditions, ice thickness and oscillation period.

While approximations to the Stokes equations have dominated ice-sheet modelling for decades, full-Stokes ice-sheet models have become more common in prognostic and diagnostic studies (Durand et al. 2009b; Zhang et al. 2011; Petra et al. 2012; Seddik et al. 2012; Seroussi et al. 2012; Isaac, Stadler & Ghattas 2015; Gagliardini et al. 2016; Zhu et al. 2016; Helanow & Ahlkrona 2018). In contrast to existing approaches to full-Stokes grounding-line dynamics, we resolve the contact conditions directly during solution of the variational problem (Durand et al. 2009a; Favier et al. 2012; Cheng et al. 2020). Not only does this result in a simple numerical method, but also the penalty-method solution is known to converge to the solution of the underlying variational inequality problem. The penalty method (3.21) can be implemented in existing finite-element marine ice-sheet models by simply (i) extending the water pressure weak form inland of the grounding line and (ii) adding the penalty weak form. Moreover, the method does not introduce additional numerical constraints on stability or resolution beyond those already necessary for time-accurate free-surface Stokes solutions.

The penalty method developed herein is perhaps the simplest variational treatment of the contact conditions. Alternative methods that possess improved convergence properties probably exist. Defining an effective stress $\sigma_e = \sigma_n - p_w$, the contact conditions (2.27) are equivalent to the single equation

$$\sigma_e = \max(0, \sigma_e + \varepsilon^{-1} u_n), \tag{5.1}$$

for arbitrary $\varepsilon > 0$. The penalty method can be derived from (5.1) by dropping the σ_{e} inside the max function and carrying through a derivation similar to § 3.1, but testing against functions $v \in V_D$. Advanced methods that instead solve (5.1) iteratively have been developed for the classical Signorini problem (Stadler 2007; Ito & Kunisch 2008).

6. Conclusions

Here, we have introduced variational formulations of contact problems for marine ice sheets and subglacial lakes. These models take the form of variational inequalities that are analogous to the Signorini problem from elasticity. The formulations can be extended naturally in several pertinent directions since the contact conditions are independent of constitutive relations on the stress and water pressure. For example, the method can be extended to include (i) a dynamic water pressure near the grounding line if ice flow is coupled to a subglacial hydrology model, (ii) an elastic or viscoelastic ice rheology or (iii) complex bed geometry. Therefore, the contact formulations developed herein are widely applicable to future work on the interaction between grounding-line migration, subglacial hydrological systems, climatic forcings and ice-sheet evolution.

Supplementary movies. Supplementary movies are available at https://doi.org/10.1017/jfm.2021.394.

Acknowledgements. We thank G. Stadler (New York University), J. Kingslake (Columbia University) and M. Siegfried (Colorado School of Mines) for discussions about this work. We are grateful for suggestions from three anonymous reviewers that improved the quality and clarity of the article.

Funding. A.G.S. was supported by a National Science Foundation Graduate Research Fellowship. A.G.S. thanks E. Bueler (University of Alaska) for introduction to free-surface Stokes problems during University of Alaska's 2018 International Summer School in Glaciology. T.T.C. was supported by the Vetlesen Foundation and NSF grant OPP-1643970.

Declaration of interests. The authors report no conflict of interest.

Author ORCIDs.

Aaron G. Stubblefield https://orcid.org/0000-0003-3949-934X.

Appendix A. Well-posedness lemmas

A.1. Function space setting

For $\hat{r} \geqslant 1$ and a set O, we define the norms $\|\Phi\|_{L^{\hat{r}}(O)} = (\int_{O} |\Phi|^{\hat{r}})^{1/\hat{r}}$, where $|\cdot|$ denotes the absolute value of a scalar, Euclidean norm of a vector, or Frobenius norm of a tensor. We define the function space for velocity V to be the completion of $C^1(\Omega)$ with respect to the norm

$$\|\mathbf{v}\|_{V} = \|\mathbf{v}\|_{W^{1,r}(\Omega)} + \|v_n\|_{L^2(\Gamma_c)}.$$
 (A1)

The Sobolev norm $\|\mathbf{v}\|_{W^{1,r}(\Omega)} = (\|\mathbf{v}\|_{L^r(\Omega)}^r + \|\nabla \mathbf{v}\|_{L^r(\Omega)}^r)^{1/r}$ in (A1) ensures that the weak forms of the flow law (2.9) and sliding law (2.25) are well defined (Jouvet & Rappaz 2011; Chen et al. 2013). The additional L^2 norm over Γ_s in (A1) ensures that the weak forms of the water pressures (2.14) and (2.17) are well-defined. A similar setting arises when using a linear sliding law (Isaac et al. 2015). We let $Q = L^{r'}(\Omega)$ be the function space for the ice pressure, where r' = r/(r-1) is the Hölder conjugate of r.

A.2. Properties of K_{\star} and \mathcal{J}

The set K is closed and convex (Kikuchi & Oden 1988, cf. Theorem 5.7). We let $\{v_k\}$ K_{\star} with $v_k \to v \in K$ strongly as $k \to \infty$. We define $v_{k,n} = v_k \cdot n|_{\partial \Omega}$. Using Hölder's inequality and the local estimate $|\nabla \cdot u| \le \sqrt{2} |\nabla u|$, we obtain

$$|q_w \dot{\mathcal{V}} - b_\Omega(q, \mathbf{v}) - b_\Gamma(q_w, \mathbf{v})| = |b_\Omega(q, \mathbf{v}_k - \mathbf{v}) + b_\Gamma(q_w, \mathbf{v}_k - \mathbf{v})| \tag{A2}$$

$$\leq \sqrt{2} \|q\|_{Q} \|\boldsymbol{v}_{k} - \boldsymbol{v}\|_{W^{1,r}(\Omega)} + |q_{w}| |\Gamma_{s}|^{\frac{1}{2}} \|v_{k,n} - v_{n}\|_{L^{2}(\Gamma_{s})}$$
(A3)

$$\leq \max(\sqrt{2}\|q\|_{Q}, |q_{w}||\Gamma_{s}|^{\frac{1}{2}}) \times \|v_{k} - v\|_{V} \to 0$$
 (A4)

as $k \to \infty$, for all $(q, q_w) \in Q \times \mathbb{R}$. Therefore, $v \in K_{\star}$ and K_{\star} is closed.

Next, we show that \mathcal{J} is continuous and coercive with respect to the norm $\|\mathbf{v}\|_V = \|\mathbf{v}\|_{W^{1,r}(\Omega)} + \|v_n\|_{L^2(\Gamma_s)}$. To leverage previous results, we define $\hat{\mathcal{J}}(\mathbf{v}) = \mathcal{J}(\mathbf{v})$ $\rho_w g \int_{\Gamma_n} \gamma_1 v_n^2 + (\gamma_2 - s) v_n ds$. Continuity of \mathcal{J} follows from continuity of $\hat{\mathcal{J}}$ with respect to $\|\cdot\|_{W^{1,r}(\Omega)}$ and continuity of $\int_{\Gamma_s} \gamma_1 v_n^2 + (\gamma_2 - s) v_n ds$ with respect to $\|\cdot\|_{L^2(\Gamma_s)}$ (Chen et al. 2013, Lemmas 9 and 12). Coercivity of $\hat{\mathcal{J}}$ on $W^{1,r}(\Omega)$ is guaranteed by

$$\hat{\mathcal{J}}(\boldsymbol{v}) \geqslant c_1 \|\boldsymbol{v}\|_{W^{1,r}(\Omega)} - c_2 \tag{A5}$$

for some positive constants c_1 and c_2 , provided that $\|\mathbf{v}\|_{W^{1,r}(\Omega)}$ is sufficiently large and $\Gamma_b \neq \emptyset$ (Chen et al. 2013, Lemma 13). We use Hölder's inequality to estimate

$$\rho_{w}g \int_{\Gamma_{s}} \gamma_{1}v_{n}^{2} + (\gamma_{2} - s)v_{n} \,ds \geqslant c_{3} \|v_{n}\|_{L^{2}(\Gamma_{s})}^{2} - c_{4} \|v_{n}\|_{L^{2}(\Gamma_{s})}, \tag{A6}$$

where $c_3 = \rho_w g \gamma_1$ and $c_4 = \rho_w g \| \gamma_2 - s \|_{L^2(\Gamma_s)}$. Combining (A5) and (A6), we obtain

$$\mathcal{J}(\mathbf{v}) \geqslant c_1 \|\mathbf{v}\|_{W^{1,r}(\Omega)} + c_3 \|v_n\|_{L^2(\Gamma_s)}^2 - c_4 \|v_n\|_{L^2(\Gamma_s)} - c_2, \tag{A7}$$

which shows that $\mathcal{J}(\boldsymbol{v}) \to \infty$ when $\|\boldsymbol{v}\|_V \to \infty$.

Marine ice-sheet and subglacial-lake grounding-line

A.3. Existence and uniqueness of the pressures

Here, we prove the existence and the uniqueness of the ice pressure p and mean water pressure \bar{p}_w in the mixed formulation (3.12) given a solution $u \in K_{\star}$ to the reduced formulation (3.14). In the following, we show that the problem involves test functions belonging to

$$V_0 = \{ \boldsymbol{v} \in V : \ \boldsymbol{v} = \boldsymbol{0} \text{ on } \Gamma_b \cup \Gamma_D \}. \tag{A8}$$

Following Isaac *et al.* (2015), we define the subspace $\tilde{V}_0 = \{ v \in V_0 : v_n |_{\Gamma_s} = 0 \}$ where the norm reduces to $\|v\|_V = \|v\|_{W^{1,r}(\Omega)}$. Using the inf-sup condition (Lemma 3.9) from Jouvet & Rappaz (2011) on \tilde{V}_0 , we obtain

$$\sup_{\boldsymbol{u}\in V_0} \frac{b_{\Omega}(q,\boldsymbol{u})}{\|\boldsymbol{u}\|_{V}} \geqslant \sup_{\boldsymbol{u}\in \tilde{V}_0} \frac{b_{\Omega}(q,\boldsymbol{u})}{\|\boldsymbol{u}\|_{V}} \geqslant c_6 \|q\|_{Q}$$
(A9)

for all $q \in Q$, where c_6 is a positive constant. We choose an arbitrary $\xi \in V_0$ such that $\nabla \cdot \boldsymbol{\xi} = 0, \, \xi_n \geqslant 0$ on Γ_w and $c_7 = \|\xi_n\|_{L^1(\Gamma_s)} / \|\boldsymbol{\xi}\|_V > 0$. For example, $\boldsymbol{\xi}$ can be obtained as the solution of an auxiliary Stokes problem posed over V_0 , with ξ_n prescribed on Γ_w . The constraint operator b_{Γ} then satisfies the inf–sup condition

$$\sup_{\boldsymbol{u} \in V_0, \, \nabla \cdot \boldsymbol{u} = 0} \frac{b_{\Gamma}(q_w, \boldsymbol{u})}{\|\boldsymbol{u}\|_V} \geqslant c_7 |q_w| \tag{A10}$$

for all $q_w \in \mathbb{R}$. We define the combined volume-change and incompressibility constraint operator

$$b(q_w, q, \mathbf{u}) = b_{\Omega}(q, \mathbf{u}) + b_{\Gamma}(q_w, \mathbf{u}). \tag{A11}$$

The inf-sup conditions (A9) and (A10) imply that

$$\sup_{\mathbf{u} \in V_0} \frac{b(q_w, q, \mathbf{u})}{\|\mathbf{u}\|_V} \geqslant c_8(\|q\|_Q + |q_w|) \tag{A12}$$

for some $c_8 > 0$ (Howell & Walkington 2011, Theorem 3.1).

In the following, we show that any $v \in K$ can be expressed as

$$\mathbf{v} = \tilde{\mathbf{v}} + \boldsymbol{\varphi} \quad \text{for } \tilde{\mathbf{v}} \in K_{\star}, \quad \boldsymbol{\varphi} \in V_0.$$
 (A13)

We substitute the decomposition (A13) into (3.12) to obtain

$$\mathcal{F}(\boldsymbol{u}, \tilde{\boldsymbol{v}} - \boldsymbol{u}) + \mathcal{P}_{\boldsymbol{w}}^{l}(\boldsymbol{u}, \tilde{\boldsymbol{v}} - \boldsymbol{u}) + \mathcal{F}(\boldsymbol{u}, \boldsymbol{\varphi}) + \mathcal{P}_{\boldsymbol{w}}^{l}(\boldsymbol{u}, \boldsymbol{\varphi}) + b(\bar{p}_{\boldsymbol{w}}, p, \boldsymbol{\varphi}) \geqslant 0.$$
 (A14)

As we found a unique $u \in K_{\star}$ satisfying (3.14) for all $\tilde{v} \in K_{\star}$, the problem reduces to finding $(p, \bar{p}_w) \in Q \times \mathbb{R}$ such that

$$b(\bar{p}_w, p, \varphi) = -\mathcal{F}(\boldsymbol{u}, \varphi) - \mathcal{P}_w^l(\boldsymbol{u}, \varphi)$$
(A15)

for all $\varphi \in V_0$. We define the kernel of b over V_0 by $\ker(b) = \{ \varphi \in V_0 : b(q_w, q, \varphi) = \varphi \in V_0 \}$ 0 for all $(q, q_w) \in Q \times \mathbb{R}$. Setting $v = u \pm \varphi_0$ for $\varphi_0 \in \ker(b)$ in (3.14), we find that

$$\mathcal{F}(\boldsymbol{u}, \boldsymbol{\varphi}_0) + \mathcal{P}_w^l(\boldsymbol{u}, \boldsymbol{\varphi}_0) = 0 \tag{A16}$$

for all $\varphi_0 \in \ker(b)$. As both sides of (A15) vanish for $\varphi_0 \in \ker(b)$, we resort to the quotient space $V_0/\ker(b)$. Hölder's inequality and (A16) show that $\mathcal{F}(u,\cdot) + \mathcal{P}_w^l(u,\cdot)$ is a bounded linear functional over $V_0/\text{ker}(b)$ (Conway 2007, Theorem 10.2). Therefore, the inf–sup



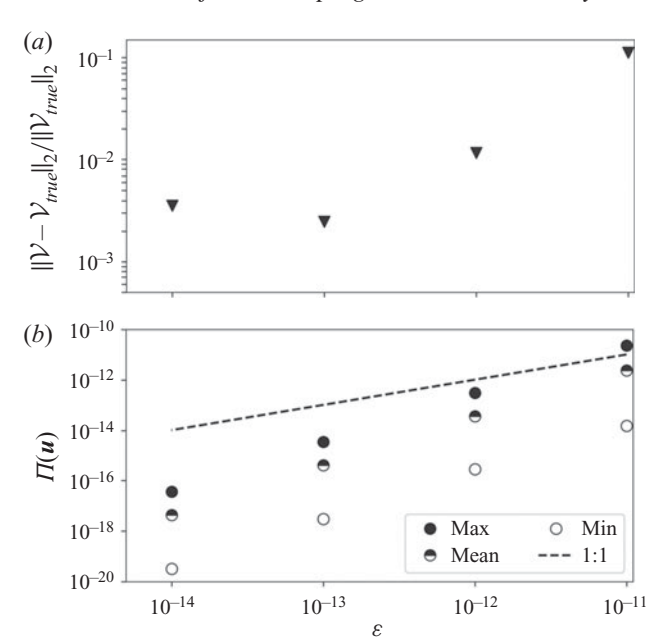


Figure 7. (a) Convergence of volume change V(t) towards the exact value $V_{true}(t)$ with decreasing penalty parameter ε . (b) Maximum, minimum and average values of the penalty functional over the simulation time, showing that $\Pi(u) \to 0$ faster than $\varepsilon \to 0$. The time-step size and element width at the lower boundary are $\Delta t = 1/2000$ yr and $\Delta x = 12.5$ m, respectively.

condition (A12) and generalised Lax-Milgram theorem guarantee that a unique solution $(p, \bar{p}_w) \in O \times \mathbb{R}$ to (A15) exists (Howell & Walkington 2011, Theorem 2.1).

Now we show that the vector decomposition (A13) holds. We denote the subset of admissible velocity fields that obey the volume change constraint by $K_{\circ} = \{ v \in K : -\int_{\Gamma_s} v_n \, ds = V \}$. Using Lemma 3.3 from Amrouche & Girault (1994), we can write any $\mathbf{v}_{\circ} \in K_{\circ}$ as $\mathbf{v}_{\circ} = \tilde{\mathbf{v}} + \psi$, where $\tilde{\mathbf{v}} \in K_{\star}$ and $\psi \in V$ with $\psi = \mathbf{0}$ on $\Gamma_{s} \cup \Gamma_{D}$ (Chen et al. 2013, cf. § 4). We choose an arbitrary $\xi' \in V_0$ satisfying $\int_{\Gamma_0} \xi'_n ds \neq 0$. Then, for any $\mathbf{v} \in K$ we have that $\mathbf{v}_{\circ} = \mathbf{v} - \lambda \boldsymbol{\xi}'$ is in K_{\circ} , where $\lambda = (\dot{\mathcal{V}} + \int_{\Gamma_s} v_n \, \mathrm{d}s) / \int_{\Gamma_{v_s}} \xi_n' \, \mathrm{d}s$. The decomposition (A13) then follows with $\varphi = \psi + \lambda \xi'$

Appendix B. Numerical tests

B.1. Convergence tests

Here, we test the convergence of the numerical method with decreasing penalty parameter ε , time-step size Δt and element width at the lower boundary Δx . We assume the same subglacial-lake set-up as in § 4.2. We choose a final time of one year, corresponding to a single filling-draining cycle. First, we study convergence with decreasing ε by comparing the exact volume change $\mathcal{V}_{\text{true}}(t)$ with the computed volume change $\mathcal{V}(t)$. We observe that the relative error $\|\mathcal{V}_{true} - \mathcal{V}\|_2 / \|\mathcal{V}_{true}\|_2 < 10^{-2}$ when $\varepsilon \lesssim 10^{-13}$ (figure 7a). The average value of the penalty functional $\Pi(u)$ over the simulation time is more than an order of magnitude smaller than ε when $\varepsilon \lesssim 10^{-12}$ (figure 7b).

We define the CFL number $\kappa = x_g' \Delta t / \Delta x$, where x_g' is the maximum grounding-line speed associated with the fine-resolution simulation ($\Delta x = 12.5$ m and $\Delta t = 1/2000$ yr). As Δx decreases, we observe that $\|\mathcal{V}_{true} - \mathcal{V}\|_2 / \|\mathcal{V}_{true}\|_2$ converges approximately

Marine ice-sheet and subglacial-lake grounding-line

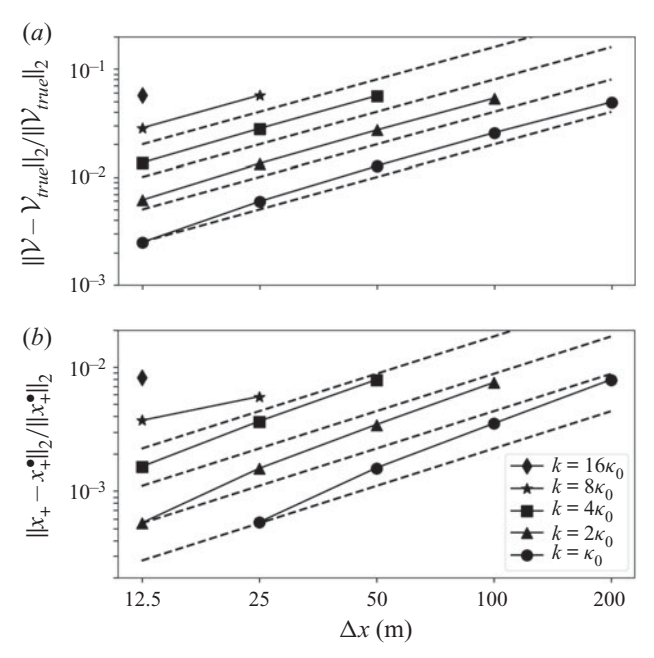


Figure 8. (a) Convergence of volume change V(t) to the exact value $V_{true}(t)$ with decreasing element width at the lower boundary Δx for different CFL numbers $\kappa := x'_{\varrho} \Delta t / \Delta x$, where x'_{ϱ} is the maximum grounding-line speed for the fine-resolution simulation ($\Delta x = 12.5$ m and $\Delta t = 1/2000$ yr). The CFL number $\kappa_0 \approx 0.96$ corresponds to the black circles. (b) Convergence of the grounding-line position $x_+(t)$ to the fine-resolution position $x_{+}^{\bullet}(t)$ ($\Delta x = 12.5$ m and $\Delta t = 1/2000$ yr) as Δx decreases for different CFL numbers. Linear convergence in Δx and Δt are noted by the black dashed lines in (a,b). The penalty parameter is $\varepsilon = 10^{-13}$.

linearly (figure 8a). Convergence with decreasing Δt (decreasing κ) is also approximately linear. To study convergence of the grounding-line position $x_+(t)$, we define $x_+^{\bullet}(t)$ to be the fine-resolution solution. We observe that $||x_+ - x_+^{\bullet}||_2/||x_+^{\bullet}||_2$ decreases approximately linearly for larger values of Δx and Δt (figure 8b). Convergence at smaller $(\Delta x, \Delta t)$ becomes superlinear because $x_+ \to x_+^{\bullet}$ when $(\Delta x, \Delta t) \to (12.5 \text{ m}, 1/2000 \text{ yr})$. We also provide time series of V/V_0 and x_+ for $\kappa = \kappa_0$ and a range of element widths (figure 9).

B.2. Triangular-lake benchmark

Here, we provide an additional benchmark test for validation. We rely on the expectation that the ice-water surface should remain nearly flat if the lake volume changes sufficiently slowly. We consider a wedge-shaped bed with slope m = 1/500 given by $\beta(x) = m|x|$, and an initial lower surface $s(x, 0) = \max(\beta(x), s_0)$ where $s_0 = 5/2$ m is constant, resulting in a triangular-initial-lake geometry. We suppose that the ice-water surface evolves as

$$s(x,t) = s_0 + \dot{s}t \quad \text{(for } s > \beta), \tag{B1}$$

where \dot{s} is a constant uplift rate. In this case, the grounding-line positions are given by

$$x_{\pm}(t) = \pm \frac{s_0 + \dot{s}\,t}{m}.$$
 (B2)

The volume change associated with (B1) and (B2) is given by $V(t) = V_0(1 + (\dot{s}/s_0)t)^2$, where V_0 is the initial volume. We provide the associated volume change rate $\dot{V}(t) =$ $2\mathcal{V}_0 \dot{s}/s_0 (1+(\dot{s}/s_0)t)$ as input in the numerical tests for various values of \dot{s} (figure 10).

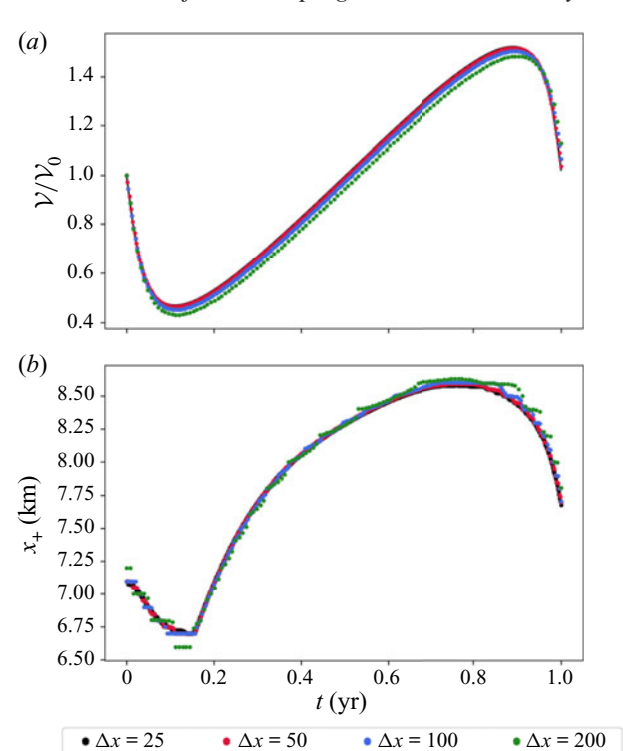


Figure 9. (a) Volume change and (b) grounding-line position time series with a CFL number of $\kappa = \kappa_0 \approx 0.96$ over a range of Δx . The penalty parameter is $\varepsilon = 10^{-13}$ for all simulations.

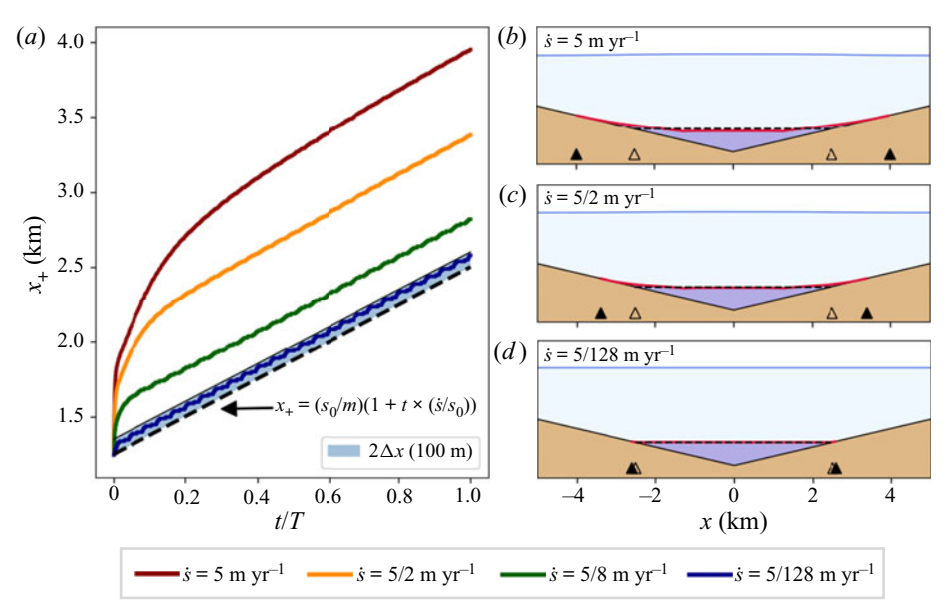


Figure 10. (a) Convergence of x_+ towards the expected slow-filling solution ((B2), dashed line) as \dot{s} becomes small. The final time T is related to the filling rate by $T = s_0/\dot{s}$. (b,c) Free-surface plots for larger values of \dot{s} at the final time. (d) Free-surface plot for small s at the final time. The grounding lines (black triangles) and ice-water elevation (red line) are close to the asymptotic solutions ((B2), open triangles) and ((B1), dashed line), respectively. For all simulations, $\Delta x = 50$ m, $\Delta t = 10^{-3}$ yr and $\varepsilon = 10^{-14}$.

We set $\dot{s} = s_0/T$ and vary the final time T so that the total water volume change is always the same. In the slow-filling limit ($\dot{s} \lesssim 5/128 \text{ m yr}^{-1}$), the numerical grounding-line position remains within $2\Delta x$ of the asymptotic solution (figure 10a). The small discrepancy arises because a rapid initial adjustment causes the ice-water surface to meet the bed tangentially whenever $\dot{s} > 0$; this effect also occurs in a similar model of subglacial cavitation (Fowler 1986; Schoof 2005). At fast filling rates, a crack-like geometry develops near the grounding lines as they rapidly migrate outwards (figure 10b,c). At slower filling rates, the ice-water surface remains flat and approaches the asymptotic solution (B1).

REFERENCES

- ALNÆS, M.S., BLECHTA, J., HAKE, J., JOHANSSON, A., KEHLET, B., LOGG, A., RICHARDSON, C., RING, J., ROGNES, M.E. & WELLS, G.N. 2015 The FEniCS Project Version 1.5. Arch. Numer. Softw. 3 (100), 9-23.
- AMROUCHE, C. & GIRAULT, V. 1994 Decomposition of vector spaces and application to the Stokes problem in arbitrary dimension. Czech. Math. J. 44 (1), 109-140.
- BRUNT, K.M., FRICKER, H.A. & PADMAN, L. 2011 Analysis of ice plains of the Filchner-Ronne Ice Shelf, Antarctica, using ICESat laser altimetry. J. Glaciol. 57 (205), 965–975.
- BRUNT, K.M., FRICKER, H.A., PADMAN, L., SCAMBOS, T.A. & O'NEEL, S. 2010 Mapping the grounding zone of the Ross Ice Shelf, Antarctica, using ICESat laser altimetry. Ann. Glaciol. 51 (55), 71–79.
- CHEN, Q., GUNZBURGER, M. & PEREGO, M. 2013 Well-posedness results for a nonlinear Stokes problem arising in glaciology. SIAM J. Math. Anal. 45 (5), 2710–2733.
- CHENG, G., LÖTSTEDT, P. & VON SYDOW, L. 2020 A full stokes subgrid scheme in two dimensions for simulation of grounding line migration in ice sheets using elmer/ice (v8.3). Geosci. Model Dev. 13 (5), 2245-2258.
- CONWAY, J.B. 2007 A Course in Functional Analysis. Springer.
- CREYTS, T.T. & SCHOOF, C.G. 2009 Drainage through subglacial water sheets. J. Geophys. Res.: Earth 114 (F4), F04008.
- CUFFEY, K.M. & PATERSON, W.S.B. 2010 The Physics of Glaciers. Academic Press.
- DURAND, G., GAGLIARDINI, O., DE FLEURIAN, B., ZWINGER, T. & LE MEUR, E. 2009a Marine ice sheet dynamics: hysteresis and neutral equilibrium. J. Geophys. Res.: Sol. Ea. 114 (3), 1-10.
- DURAND, G., GAGLIARDINI, O., ZWINGER, T., LE MEUR, E. & HINDMARSH, R.C.A. 2009b Full Stokes modeling of marine ice sheets: influence of the grid size. Ann. Glaciol. 50 (52), 109–114.
- EKELAND, I. & TEMAM, R. 1999 Convex Analysis and Variational Problems. SIAM.
- FAVIER, L., DURAND, G., CORNFORD, S.L., GUDMUNDSSON, G.H., GAGLIARDINI, CHAULET, F., ZWINGER, T., PAYNE, A.J. & LE BROCQ, A.M. 2014 Retreat of Pine Island Glacier controlled by marine ice-sheet instability. Nat. Clim. Change 4 (2), 117-121.
- FAVIER, L., GAGLIARDINI, O., DURAND, G. & ZWINGER, T. 2012 A three-dimensional full Stokes model of the grounding line dynamics: effect of a pinning point beneath the ice shelf. Cryosphere 6 (1), 101–112.
- FOWLER, A.C. 1986 A sliding law for glaciers of constant viscosity in the presence of subglacial cavitation. Proc. R. Soc. Lond. A 407 (1832), 147-170.
- FOWLER, A.C. 1999 Breaking the seal at Grímsvötn, Iceland. J. Glaciol. 45 (151), 506-516.
- FOWLER, A.C. 2009 Dynamics of subglacial floods. Proc. R. Soc. Lond. A 465 (2106), 1809–1828.
- FRICKER, H.A. & PADMAN, L. 2006 Ice shelf grounding zone structure from ICESat laser altimetry. Geophys. Res. Lett. 33 (15), L15502.
- FRICKER, H.A. & SCAMBOS, T. 2009 Connected subglacial lake activity on lower Mercer and Whillans Ice Streams, West Antarctica, 2003–2008. J. Glaciol. 55 (190), 303–315.
- FÜRST, J.J., DURAND, G., GILLET-CHAULET, F., TAVARD, L., RANKL, M., BRAUN, M. & GAGLIARDINI, O. 2016 The safety band of Antarctic ice shelves. Nat. Clim. Change 6 (5), 479–482.
- GAGLIARDINI, O., BRONDEX, J., GILLET-CHAULET, F., TAVARD, L., PEYAUD, V. & DURAND, G. 2016 Impact of mesh resolution for MISMIP and MISMIP3d experiments using Elmer/Ice. Cryosphere 10 (1), 307-312.
- GAGLIARDINI, O., COHEN, D., RÅBACK, P. & ZWINGER, T. 2007 Finite-element modeling of subglacial cavities and related friction law. J. Geophys. Res.: Earth 112 (F2), F02027.
- GLEN, J.W. 1955 The creep of polycrystalline ice. Proc. R. Soc. Lond. A 228 (1175), 519–538.
- GUDLAUGSSON, E., HUMBERT, A., KLEINER, T., KOHLER, J. & ANDREASSEN, K. 2016 The influence of a model subglacial lake on ice dynamics and internal layering. Cryosphere 10 (2), 751–760.

- GUDMUNDSSON, G.H. 2007 Tides and the flow of Rutford ice stream, West Antarctica. J. Geophys. Res.: Earth 112 (F4), F04007.
- GUDMUNDSSON, G.H., KRUG, J., DURAND, G., FAVIER, L. & GAGLIARDINI, O. 2012 The stability of grounding lines on retrograde slopes. Cryosphere 6 (6), 1497–1505.
- HELANOW, C. & AHLKRONA, J. 2018 Stabilized equal low-order finite elements in ice sheet modeling accuracy and robustness. Comput. Geosci. 22 (4), 951-974.
- HEWITT, I.J., SCHOOF, C. & WERDER, M.A. 2012 Flotation and free surface flow in a model for subglacial drainage. Part 2. Channel flow. J. Fluid Mech. 702, 157–187.
- HOWELL, J.S. & WALKINGTON, N.J. 2011 Inf-sup conditions for twofold saddle point problems. Numer. Math. 118 (4), 663-693.
- ISAAC, T., STADLER, G. & GHATTAS, O. 2015 Solution of nonlinear Stokes equations discretized by high-order finite elements on nonconforming and anisotropic meshes, with application to ice sheet dynamics. SIAM J. Sci. Comput. 37 (6), B804-B833.
- ITO, K. & KUNISCH, K. 2008 Semi-smooth Newton methods for the Signorini problem. Appl. Maths 53 (5), 455-468.
- JOUGHIN, I., SMITH, B.E. & MEDLEY, B. 2014 Marine ice sheet collapse potentially under way for the Thwaites Glacier Basin, West Antarctica. Science 344 (6185), 735–738.
- JOUVET, G. & RAPPAZ, J. 2011 Analysis and finite element approximation of a nonlinear stationary Stokes problem arising in glaciology. Adv. Numer. Anal. 2011, 164581.
- KAMB, B. 1970 Sliding motion of glaciers: theory and observation. Rev. Geophys. 8 (4), 673–728.
- KIKUCHI, N. & ODEN, J.T. 1988 Contact Problems in Elasticity: A Study of Variational Inequalities and Finite Element Methods. SIAM.
- KINGSLAKE, J. 2015 Chaotic dynamics of a glaciohydraulic model. J. Glaciol. 61 (227), 493-502.
- LOGG, A., MARDAL, K.-A. & WELLS, G.N. 2012 Automated Solution of Differential Equations by the Finite Element Method. Springer.
- LOGG, A. & WELLS, G.N. 2010 DOLFIN: automated finite element computing. ACM Trans. Math. Softw. 37 (2), 20.
- MACAYEAL, D.R. 1989 Large-scale ice flow over a viscous basal sediment: theory and application to ice stream B, Antarctica. J. Geophys. Res. 94 (B4), 4071–4087.
- MILILLO, P., RIGNOT, E., RIZZOLI, P., SCHEUCHL, B., MOUGINOT, J., BUESO-BELLO, J. & PRATS-IRAOLA, P. 2019 Heterogeneous retreat and ice melt of Thwaites Glacier, West Antarctica. Sci. Adv. 5 (1), eaau3433.
- MUSZYNSKI, I. & BIRCHFIELD, G.E. 1987 A coupled marine ice-stream-ice-shelf model. J. Glaciol. 33 (113), 3-15.
- NYE, J.F. 1976 Water flow in glaciers: jökulhlaups, tunnels and veins. J. Glaciol. 17 (76), 181–207.
- PAOLO, F.S., FRICKER, H.A. & PADMAN, L. 2015 Volume loss from Antarctic ice shelves is accelerating. Science 348 (6232), 327-331.
- PATTYN, F. 2008 Investigating the stability of subglacial lakes with a full Stokes ice-sheet model. J. Glaciol. **54** (185), 353–361.
- PEGLER, S.S. 2018 Marine ice sheet dynamics: the impacts of ice-shelf buttressing. J. Fluid Mech. 857, 605-647.
- PEGLER, S.S., KOWAL, K.N., HASENCLEVER, L.Q. & WORSTER, M.G. 2013 Lateral controls on grounding-line dynamics. J. Fluid Mech. 722, R1.
- PEGLER, S.S. & WORSTER, M.G. 2013 An experimental and theoretical study of the dynamics of grounding lines. J. Fluid Mech. **728**, 5–28.
- PETRA, N., ZHU, H., STADLER, G., HUGHES, T.J.R. & GHATTAS, O. 2012 An inexact Gauss-Newton method for inversion of basal sliding and rheology parameters in a nonlinear Stokes ice sheet model. J. Glaciol. 58 (211), 889–903.
- RIBE, N.M. 2001 Bending and stretching of thin viscous sheets. J. Fluid Mech. 433, 135–160.
- RIGNOT, E., MOUGINOT, J., MORLIGHEM, M., SEROUSSI, H. & SCHEUCHL, B. 2014 Widespread, rapid grounding line retreat of Pine Island, Thwaites, Smith, and Kohler glaciers, West Antarctica, from 1992 to 2011. Geophys. Res. Lett. 41 (10), 3502–3509.
- ROBEL, A.A., TSAI, V.C., MINCHEW, B. & SIMONS, M. 2017 Tidal modulation of ice shelf buttressing stresses. Ann. Glaciol. 58 (74), 12–20.
- ROBISON, R.A.V., HUPPERT, H.E & WORSTER, M.G. 2010 Dynamics of viscous grounding lines. J. Fluid Mech. 648, 363-380.
- ROSIER, S. & GUDMUNDSSON, H. 2020 Exploring mechanisms responsible for tidal modulation in flow of the Filchner–Ronne Ice Shelf. Cryosphere 14 (1), 17–37.
- ROSIER, S., GUDMUNDSSON, H. & GREEN, J.A.M 2014 Insights into ice stream dynamics through modelling their response to tidal forcing. Cryosphere 8 (5), 1763–1775.

Marine ice-sheet and subglacial-lake grounding-line

- SAYAG, R. & WORSTER, M.G. 2013 Elastic dynamics and tidal migration of grounding lines modify subglacial lubrication and melting. *Geophys. Res. Lett.* 40 (22), 5877–5881.
- SCHOOF, C. 2005 The effect of cavitation on glacier sliding. Proc. R. Soc. Lond. A 461 (2055), 609-627.
- SCHOOF, C. 2007a Ice sheet grounding line dynamics: steady states, stability, and hysteresis. *J. Geophys. Res.:* Earth 112 (3), F03S28.
- SCHOOF, C. 2007b Marine ice-sheet dynamics. Part 1. The case of rapid sliding. J. Fluid Mech. 573 (February), 27–55.
- SCHOOF, C. 2011 Marine ice sheet dynamics. Part 2. A Stokes flow contact problem. *J. Fluid Mech.* **679**, 122–155.
- SCHOOF, C. 2012 Marine ice sheet stability. J. Fluid Mech. 698, 62-72.
- SCHOOF, C., HEWITT, I.J. & WERDER, M.A. 2012 Flotation and free surface flow in a model for subglacial drainage. Part 1. Distributed drainage. *J. Fluid Mech.* **702**, 126–156.
- SEDDIK, H., GREVE, R., ZWINGER, T., GILLET-CHAULET, F. & GAGLIARDINI, O. 2012 Simulations of the Greenland ice sheet 100 years into the future with the full Stokes model Elmer/Ice. *J. Glaciol.* **58** (209), 427–440.
- SERGIENKO, O.V., MACAYEAL, D.R. & BINDSCHADLER, R.A. 2009 Stick-slip behavior of ice streams: modeling investigations. *Ann. Glaciol.* **50** (52), 87–94.
- SEROUSSI, H., DHIA, H.B., MORLIGHEM, M., LAROUR, E., RIGNOT, E. & AUBRY, D. 2012 Coupling ice flow models of varying orders of complexity with the Tiling method. *J. Glaciol.* **58** (210), 776–786.
- SEROUSSI, H., MORLIGHEM, M., LAROUR, E., RIGNOT, E. & KHAZENDAR, A. 2014 Hydrostatic grounding line parameterization in ice sheet models. *Cryosphere* **8** (6), 2075–2087.
- SIEGFRIED, M.R. & FRICKER, H.A. 2018 Thirteen years of subglacial lake activity in Antarctica from multi-mission satellite altimetry. Ann. Glaciol. 59, 42–55.
- SMITH, B.E., FRICKER, H.A., JOUGHIN, I.R. & TULACZYK, S. 2009 An inventory of active subglacial lakes in Antarctica detected by ICESat (2003–2008). J. Glaciol. 55 (192), 573–595.
- SMITH, B.E., GOURMELEN, N., HUTH, A. & JOUGHIN, I. 2017 Connected subglacial lake drainage beneath Thwaites Glacier, West Antarctica. *Cryosphere* 11 (1), 451–467.
- STADLER, G. 2007 Path-following and augmented Lagrangian methods for contact problems in linear elasticity. *J. Comput. Appl. Maths* **203** (2), 533–547.
- STUBBLEFIELD, A. 2020 agstub/grounding-line-methods: first release of full-Stokes grounding line dynamics solver. *J. Fluid Mech.* doi:10.5281/zenodo.4302610.
- STUBBLEFIELD, A.G., CREYTS, T.T., KINGSLAKE, J. & SPIEGELMAN, M. 2019 Modeling oscillations in connected glacial lakes. *J. Glaciol.* **65** (253), 745–758.
- SYKES, H.J., MURRAY, T. & LUCKMAN, A. 2009 The location of the grounding zone of Evans Ice Stream, Antarctica, investigated using SAR interferometry and modelling. *Ann. Glaciol.* **50** (52), 35–40.
- WALDER, J.S. & FOWLER, A. 1994 Channelized subglacial drainage over a deformable bed. *J. Glaciol.* **40** (134), 3–15.
- WARBURTON, K.L.P, HEWITT, D.R. & NEUFELD, J.A. 2020 Tidal grounding-line migration modulated by subglacial hydrology. *Geophys. Res. Lett.* 47 (17), e2020GL089088.
- WEERTMAN, J. 1957 On the sliding of glaciers. J. Glaciol. 3 (21), 33–38.
- WEERTMAN, J. 1974 Stability of the junction of an ice sheet and an ice shelf. J. Glaciol. 13 (67), 3–11.
- WRIGHT, A. & SIEGERT, M. 2012 A fourth inventory of Antarctic subglacial lakes. *Antarct. Sci.* 24 (6), 659–664.
- ZHANG, H., JU, L., GUNZBURGER, M., RINGLER, T. & PRICE, S. 2011 Coupled models and parallel simulations for three-dimensional full-Stokes ice sheet modeling. *Numer. Math.: Theory Me.* 4 (3), 396–418
- ZHU, H., PETRA, N., STADLER, G., ISAAC, T., HUGHES, T.J.R. & GHATTAS, O. 2016 Inversion of geothermal heat flux in a thermomechanically coupled nonlinear Stokes ice sheet model. *Cryosphere* 10 (4), 1477–1494.